On the Anomalous Counterclockwise Turning of the Surface Wind with Time in the Plains of the United States

HOWARD B. BLUESTEIN

School of Meteorology, University of Oklahoma, Norman, Oklahoma

GLEN S. ROMINE AND RICHARD ROTUNNO

National Center for Atmospheric Research, Boulder, Colorado

DYLAN W. REIF

School of Meteorology, University of Oklahoma, Norman, Oklahoma

CHRISTOPHER C. WEISS

Department of Geosciences, Texas Tech University, Lubbock, Texas

(Manuscript received 11 October 2017, in final form 6 December 2017)

ABSTRACT

Vertical shear in the boundary layer affects the mode of convective storms that can exist if they are triggered. In western portions of the southern Great Plains of the United States, vertical shear, in the absence of any transient features, changes diurnally in a systematic way, thus leading to a preferred time of day for the more intense modes of convection when the shear, particularly at low levels, is greatest. In this study, yearly and seasonally averaged wind observations for each time of day are used to document the diurnal variations in wind at the surface and in the boundary layer, with synoptic and mesoscale features effectively filtered out. Data from surface mesonets in Oklahoma and Texas, Doppler wind profilers, instrumented tower data, and seasonally averaged wind data for each time of day from convection-allowing numerical model forecasts are used. It is shown through analysis of observations and model data that the perturbation wind above anemometer level turns in a clockwise manner with time, in a manner consistent with prior studies, yet the perturbation wind at anemometer level turns in an anomalous, counterclockwise manner with time. Evidence is presented based on diagnosis of the model forecasts that the dynamics during the early evening boundary layer transition are, in large part, responsible for the behavior of the hodographs at that time: as vertical mixing in the boundary layer diminishes, the drag on the wind at anemometer level persists, leading to rapid deceleration of the meridional component of the wind. This deceleration acts to turn the wind to the left rather than to the right, as would be expected from the Coriolis force alone.

1. Introduction

Forecasting supercells and tornadoes in supercells is a challenge, especially when the environmental conditions for them are marginal. From observational (e.g., Rasmussen and Blanchard 1998; Thompson et al. 2007) and numerical modeling studies (Weisman and Klemp 1982, 1984), we know that a necessary condition for supercell formation is that the 0–6-km wind difference (a surrogate for vertical shear) in the environment of the storm be $>\sim 18\,\mathrm{m\,s^{-1}}$. It has also been noted that tornado formation in supercells, especially that of strong tornadoes, is more likely when the low-level shear is relatively strong (i.e., $>\sim 10\,\mathrm{m\,s^{-1}}$ in the lowest 1 km; i.e., $>10^{-2}\,\mathrm{s^{-1}}$) (e.g., Brooks et al. 2003, their Fig. 3). Dowell and Bluestein (1997, their Fig. 18), for example, found enhanced horizontal (streamwise) vorticity due to vertical shear $\sim 3 \times 10^{-2}\,\mathrm{s^{-1}}$ in the lowest 444 m from in situ measurements on an instrumented tower near a tornadic supercell. Bluestein and Pazmany (2000, their Fig. 7) found horizontal vorticity due to vertical shear under 1 km of $\sim 6 \times 10^{-2}\,\mathrm{s^{-1}}$ from a velocity azimuth

Corresponding author: Howard B. Bluestein, hblue@ou.edu

DOI: 10.1175/MWR-D-17-0297.1

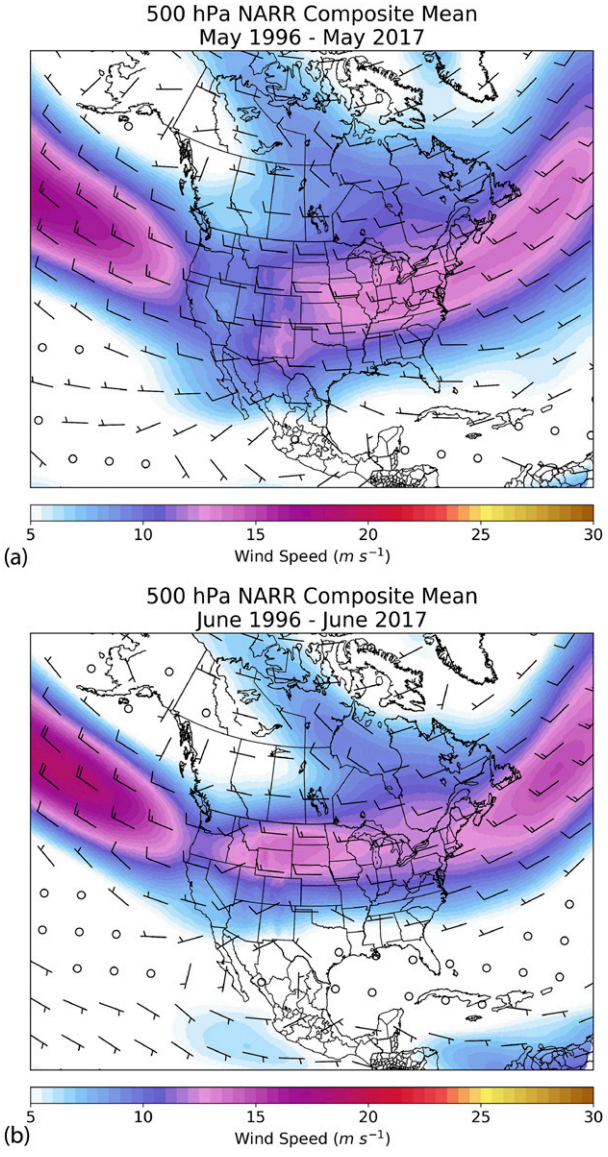

FIG. 1. Mean 500-hPa wind field for (a) May and (b) June from 1996 to 2017, based on the NCEP–NCAR reanalysis dataset. Color scale of wind speed is indicated in m s^{-1}.

display (VAD; Doviak and Zrnić 1984) based on mobile, W-band (3-mm wavelength) Doppler radar data collected just upstream from the updraft cloud base of a supercell, in which a tornado formed just 10–15 min later (Bluestein and Pazmany 2000).

Late in the severe convection season (June) in the southern Great Plains of the United States, the westerly jet of strong flow aloft migrates poleward (Fig. 1), and, therefore, the mean 0–6-km vertical shear decreases, along with the probability of supercell formation. During the past few decades, the mean westerly flow at 500 hPa, which is just under 6 km AGL, is ~12.5 m s^{-1} in Oklahoma in May and decreases to ~7.5 m s^{-1} in June. During the latter half of May into the early to middle part of June, the winds at 500 hPa are typically ~15 m s^{-1} on days when the formation of convective storms is anticipated (not shown). On these days, the easterly component of the surface wind is generally <5 m s^{-1} (not shown), so the necessary 0–6-km shear for supercell formation is either too small or marginal.

Although the vertical shear may be marginal or too weak for supercell formation early in the morning, by late afternoon, when convective initiation tends to occur, the vertical shear may increase (or at least change), owing to the following:

1) an approaching short-wave trough, which is accompanied by an increase of wind speed at 6 km AGL and/or a backing and increase in wind speed at the surface—the latter change owing to quasigeostrophic, midlevel ascent and accompanying surface convergence, a drop in the surface pressure, and an increase in the acceleration induced by the surface pressure gradient force (PGF) toward the west, east of the area of ascent (Bluestein 1992); or
2) an increase in the component of flow from higher terrain to lower terrain, resulting in the intensification of a lee trough and associated increase in the easterly component of the wind east of the trough axis; or
3) an outflow boundary created by earlier convective storms to the east, which propagates to the west (e.g., Bluestein and Pazmany 2000), from which there is a contribution to a westward-directed PGF owing to cooler air to the rear, that is, east, of the outflow boundary. This westward-directed PGF increases the easterly component to the low-level wind.

An increase in the vertical shear can be affected also by mechanisms related to mesoscale topography (assuming the winds aloft do not change), which results in changes to the wind at the surface:

1) differential heating owing to variations in cloudiness (e.g., Segal et al. 1986) and/or land use (e.g., Segal et al. 1988; Hane et al. 1997) can force a vertical, solenoidal circulation, for example, at the surface directed toward where the surface heating is greatest; or
2) heating on a sloping surface (Holton 1967) (Fig. 2), the "Holton mechanism," results in an upslope component to the wind when the surface is being heated; or
3) orogenic channeling of the surface wind (Bosart et al. 2006; Tang et al. 2016).

In addition, the following mechanisms may also change the vertical shear:

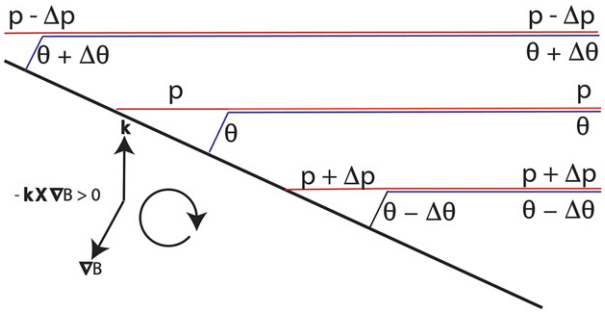

FIG. 2. Idealized schematic illustrating the solenoidal (baroclinic) generation of horizontal vorticity in the *y* direction, into the figure, through insolation on a sloped surface (thick, solid black line). The *x* direction points to the right; the *z* direction points up. Isentropes (represented as isotherms of potential temperature θ) are depicted as solid blue lines; isobars are depicted as solid red lines. Buoyancy **B** at the top of the boundary layer (where $\nabla\theta$ is directed upslope, parallel to the ground) vanishes, but in the boundary layer, $\mathbf{B} > 0$ because θ is greater than that of the environment, defined by the isentropes to the east, which are horizontal. Buoyancy **B**, therefore, increases downward and to the left in the boundary layer, where vorticity is generated as $-\mathbf{k} \times \nabla\mathbf{B}$ and **k** points upward.

1) the Coriolis force turns the surface wind to the right (in the Northern Hemisphere) when the surface flow is imbalanced, as happens when Ekman balance is disturbed if vertical mixing ceases (Blackadar 1957); and
2) turbulent vertical mixing in the boundary layer can change the surface wind speed and direction, depending on how the wind speed and direction change with height and how strong the vertical mixing is.

The former, the ''Blackadar mechanism,'' can occur when the latter weakens as the sun sets, thus inducing an inertial oscillation (Blackadar 1957).

The changes in vertical shear as a result of both the heating of sloping topography (the Holton effect) and changes in vertical mixing (the Blackadar effect) are thought responsible (e.g., Parish and Oolman 2010; Du and Rotunno 2014) for the nocturnal low-level jet (LLJ) in the plains of the United States (Bonner 1968; Bonner and Paegle 1970). The LLJ is associated with an increase in vertical shear, especially at low levels, and may play a role in the intensification of convective storms during the transition from daytime to nighttime conditions (e.g., Bluestein 2009). Storm chasers and severe-storm forecasters have noted anecdotally the tendency of ordinary cells to evolve into supercells, and of nontornadic supercells to evolve into tornadic supercells, during the late afternoon and early evening; this effect is colloquially referred to as ''six o'clock magic'' (Bluestein 2013), though it has also been informally referred to as a perceived time when convective storms are most likely to be initiated along the dryline, without regard for the nature or intensity of the convection. It has also been proposed that six o'clock magic is due to an increase in surface/low-level water vapor in response to the advection of moisture by the LLJ (W. Blumberg 2017, personal communication). However, because the six o'clock magic effect has not been proven rigorously on the basis of observations, it must be regarded with extreme caution. Nevertheless, the study to be described will attempt to quantify what changes occur in boundary layer shear around 1800 local time (i.e., late in the afternoon and early evening) and if they can have significant consequences then.

The main objective of this study is to determine how the low-level wind field evolves late in the afternoon and early in the evening in the plains of the United States under quiescent conditions (i.e., weak or no quasigeostrophic forcing, no influence of outflow boundaries, no cloudiness or land-use variations) and how it might affect the 0–6-km shear (assuming no changes in the 6-km AGL wind) and the low-level shear. The perturbation winds, defined as the difference between the wind and its long-term (for many days) mean, rotate in a clockwise manner with time above the surface, especially in the southern plains during the spring and summer (e.g., Zhong et al. 1996; Jiang et al. 2007). Considering the winds over the central Great Plains, over a long period of time, it is expected that migratory synoptic-scale disturbances and transient, mesoscale disturbances are filtered out, so that in a quiescent atmosphere, the winds at low levels but above the surface back and increase in speed with time late in the afternoon and early evening (Fig. 3). Shapiro et al. (2016) were able to reproduce this behavior using an analytic model that included both the Holton and Blackadar effects (Fig. 4). Shapiro et al. (2016) found, using parameters in their model representative of the real atmosphere, that the magnitude of the perturbation winds is greatest at 500 m AGL and decreases above and below, and that the clockwise turning with time persists up to at least 3 km and down to 1 m AGL (A. Shapiro 2017, personal communication).

While the ultimate motivation for this study is to quantify how much the 0–6-km shear and the low-level shear increase as a result of the Holton and Blackadar effects and whether or not the increases can affect the behavior of convection, the actual objectives of this study are just to determine how the perturbation wind changes with time at low levels under quiescent conditions. Whether the increases in shear are actually enough to change the behavior of convective storms is beyond the scope of this study.

This study will make use of both observations and numerical simulations, the nature of which are detailed

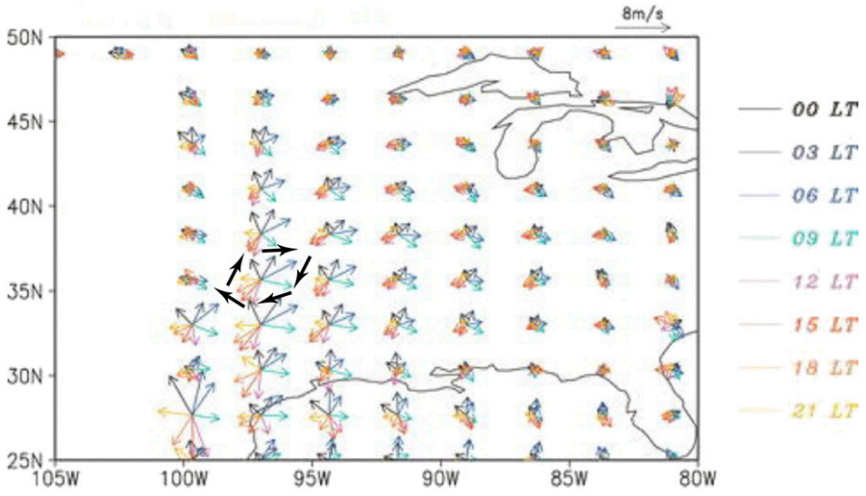

FIG. 3. Perturbation wind vectors over the eastern portion of the United States every 3 h from 25-yr mean (October 1978–December 2003) NARR data (Mesinger et al. 2006) at 925 hPa. Times (LT) for each wind vector are indicated by the color scale. The black vectors show the sense of the rotation of the perturbation winds as a function of time [adapted from Fig. 2a of Jiang et al. (2007)].

in section 2. The results from analyses of the observations and the numerical model data are presented in sections 3 and 4, respectively. Conclusions drawn from these analyses and a discussion of the results and their implications are found in section 5.

2. Methodology

This study makes use of four main sources of data: the Oklahoma Mesonet, the West Texas Mesonet (WTM), the NOAA Wind Profiler Demonstration Network (WPDN), and numerical forecasts from the Weather Research and Forecasting (WRF) Model.

a. The Oklahoma Mesonet

The Oklahoma Mesonet (http://www.mesonet.org; Brock et al. 1995; McPherson et al. 2007) is a network of instrumented, 10-m-tall towers throughout Oklahoma, with at least one site in every one of Oklahoma's 77 counties. Of relevance to this study are measurements

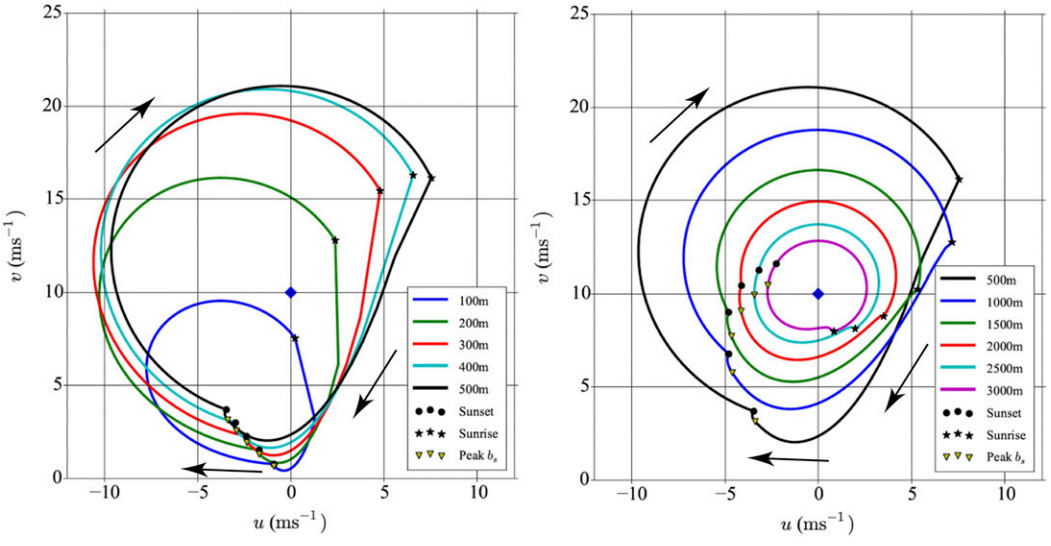

FIG. 4. Time dependence of wind hodographs at different altitudes (color coded), based on an idealized analytic model. Arrows indicate sense of rotation of perturbation wind with time [adapted from Fig. 6 of Shapiro et al. (2016)].

made of wind speed and direction at 10 m AGL every 5 min. Details about the wind-measuring instrument, including its accuracy, may be found on the Oklahoma Mesonet website and in linked publications.

b. The West Texas Mesonet

The West Texas Mesonet (http://www.depts.ttu.edu/nwi/research/facilities/wtm/index.php; Schroeder et al. 2005), which was modeled after the Oklahoma Mesonet, is a network of instrumented, 10-m-tall towers in west Texas, including the Texas Panhandle. Like the Oklahoma Mesonet, wind speed and direction are recorded as averages for every 5-min period. Details about the wind-measuring instrument, including its accuracy, may be found in Schroeder et al. (2005).

c. The NOAA Wind Profiler Demonstration Network

The now-defunct, but operational through 2014, NOAA WPDN was composed of 404.37-MHz (74.2-cm wavelength) Doppler radar wind profilers located at various locations in the central United States (Weber et al. 1990). Wind data were recorded from 500 m AGL and up based on backscatter from variations in index of refraction in clear air or from precipitation. More details about the instrumentation and its accuracy may be found in Bluestein and Speheger (1995) and in a number of references contained within this publication. For this study, hourly averaged profiler wind data were used in addition to in situ wind data at the ''surface'' (10 m) from an anemometer. Profiler and surface data were obtained from https://rda.ucar.edu/datasets/ds359.0/.

d. WRF Model forecasts

Numerical weather forecast data from the WRF (e.g., Skamarock et al. 2008; Powers et al. 2017) Model runs, known colloquially as the NCAR ensemble (Schwartz et al. 2015), were extracted from archives of daily forecasts covering the spring to summer of 2016 (forecasts initialized at 0000 UTC from 15 April to 15 August 2016). The NCAR ensemble and associated forecast data archive proved particularly fortuitous to enable preliminary investigation of results shown herein. The configuration of the model setup was identical to that documented in Schwartz et al. (2015), while the analysis system used to generate initial conditions for the forecasts includes minor changes, such as increasing the analysis ensemble size from 50 to 80 members, the addition of GPS radio occultation observations, and a spread-restoration option that slightly increases the analysis ensemble variance. Analyses are on a grid with 15-km horizontal spacing, while forecasts include a downscale initialized nest at 3-km convection-allowing horizontal grid spacing. Results shown are solely drawn from the convection-allowing nest forecasts. The initial conditions are randomly drawn from the 80-member analysis ensemble. The analysis and forecasts all have the same set of physics options: Thompson microphysics (Thompson et al. 2008), Rapid Radiative Transfer Model for GCMs (RRTMG) long- and shortwave radiation (Iacono et al. 2008), Mellor–Yamada–Janjić (MYJ) planetary boundary layer (Mellor and Yamada 1982; Janjić (1994, 2001), Noah land surface model (Chen and Dudhia 2001), and Tiedtke cumulus parameterization (Tiedtke 1989; Zhang et al. 2011). The Tiedtke cumulus parameterization was used on the outer domain only, not on the 3-km convection-allowing grid, which drew lateral boundary forcing from the associated outer domain forecast (two-way nest with 1–2–1 smoothing option). Lateral boundary conditions were also perturbed on the outer domain during forecast integration using the perturbed covariance technique of Torn et al. (2006), which adds random perturbations to the temperature, horizontal wind, and moisture. The land surface state freely evolves for each member, which adds additional diversity to the state of the boundary layer. Owing to the reliance on many parameterization schemes, the results to be described must be viewed with caution and only in a qualitative sense.

The final model forecast data used in this study are from a single ensemble member, and in particular, the wind field at the lowest and third-lowest sigma levels, whose heights (AGL) vary somewhat spatially owing to the mass-based vertical coordinate of the WRF Model. Because each analysis member is an equally likely estimate of the current state of the atmosphere (Schwartz et al. 2014), it does not matter how the members are selected, and all forecasts are equally likely outcomes. The lowest grid point is near anemometer level (approximately 28 m AGL), and winds there are considered to be at/near the surface; the third-lowest grid point is considered to be in the lower portion of the planetary boundary layer (approximately 184 m AGL). Only hourly data for 12–35-h forecasts are considered so that the model has sufficient spinup time. Unlike the real-time forecast data described above, this single-member forecast set was performed retrospectively for the same forecast period using identical initial and lateral boundary conditions, but it includes additional diagnostics of forcing terms for wind accelerations that are described in more detail later.

3. Observational data analyses

Surface wind data (10 m AGL) from the Oklahoma Mesonet were averaged for each time of day over a 22-yr period from 1995 to 2016. By averaging over the entire

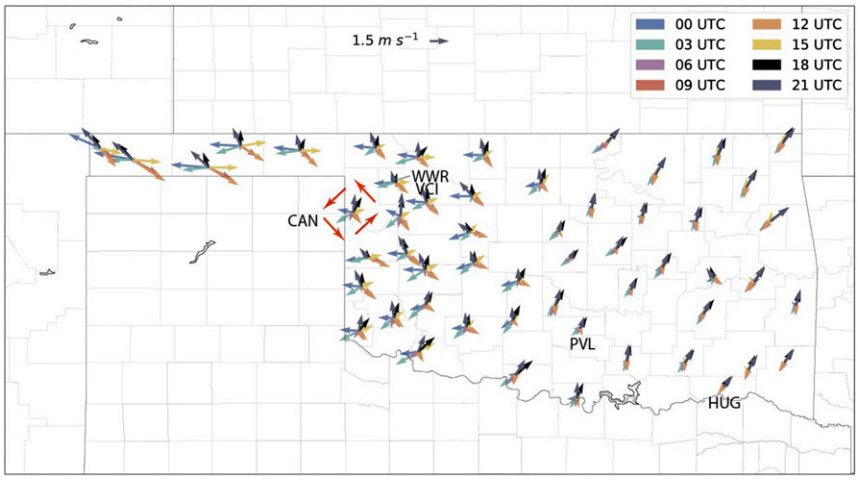

FIG. 5. Wind vectors plotted at selected stations across OK from the OK Mesonet every 3 h (color coded), averaged from 1995 to 2016. The locations of Canadian (CAN), TX (no wind vectors are plotted), Woodward (WWR), OK, Vici (VCI), OK (no wind vectors plotted), Pauls Valley (PVL), OK, and Hugo (HUG), OK, are indicated. The sense of rotation of the wind vectors with time is indicated at the site east of CAN by red arrows. Note how the winds in eastern OK vary the least with time and are either from the southwest or northeast. In western OK, the wind vectors rotate in a counterclockwise manner with time; in the western portion of the OK Panhandle, the amplitude of the variations is the greatest. Note that 1200 UTC (0000 UTC) is at 0700 CDT/0600 CST (1900 CDT/1800 CST).

year for each time of day and for such a long period of time, migratory synoptic-scale disturbances have been filtered out, and the response to diurnal heating has been averaged over the annual heating cycle. In general, the hodographs at the surface as a function of time over northwestern Oklahoma exhibited the greatest diurnal variations: $\sim 3\,\mathrm{m\,s^{-1}}$ in zonal wind and $\sim 1.5\,\mathrm{m\,s^{-1}}$ in meridional wind (Fig. 5). Unlike the hodographs of the perturbation wind from NARR data at 925 hPa (above the surface) averaged over the period from June to August from 1979 to 2003, which turned in a clockwise manner with time (Fig. 3), and unlike the hodographs in the Shapiro et al. (2016) model, the Oklahoma Mesonet perturbation-wind hodographs exhibited ''anomalous'' (Moisseeva and Steyn 2014) counterclockwise turning with time.[1]

At a site at Canadian, Texas, in the northeastern portion of the Texas Panhandle, the perturbation wind also turned in a counterclockwise manner with time (Fig. 6a); the hodograph had the same kidney bean shape as the hodograph to the east at Woodward, Oklahoma (Fig. 6b). The kidney bean shape is caused by a maximum in wind speed around local noon (1800 UTC; CST and CDT are 6 and 5 h earlier, respectively), perhaps when vertical mixing is strongest, and wind speed typically increases with height within the boundary layer; at night, the winds are weaker, owing to the loss of downward mixing of higher momentum from aloft. The sharp curves in the hodographs near sunrise and sunset are due to the onset and disappearance, respectively, of vertical mixing due to heating. It is noted that data for this station in the much newer West Texas Mesonet were averaged only over a 4-yr period, not for 22 years as were the data from the Oklahoma Mesonet, which may explain the noisier solution in Fig. 6a.

However, to the east, at Pauls Valley in south-central Oklahoma, the amplitude of the perturbations-wind oscillation in the zonal direction was much less (Fig. 6c), while in far southeastern Oklahoma, at Hugo (Fig. 6d), the amplitude was even less, only $\sim 1\,\mathrm{m\,s^{-1}}$. The sense of direction indicated in the figure, however, is consistent with that at other nearby locations (not shown), so it is not ambiguous. It appears from a terrain map of much of the southern Great Plains (Fig. 7) that mesonet sites exhibiting the highest amplitude in zonal perturbation-wind diurnal oscillation are located in a region where the zonal gradient in elevation is the greatest (cf. Figs. 5, 7). It thus appears that the amplitude of the zonal oscillation in wind perturbation seems to be related to the elevation gradient, which is suggestive of the importance of the Holton mechanism. In general circulation simulations by Jiang et al. (2007), it was

[1] Moisseeva and Steyn (2014), in a study of hodographs at a fixed height as a function of time around an island with orography, referred to this behavior as ''anomalous'' anticlockwise hodograph rotation (ACR).

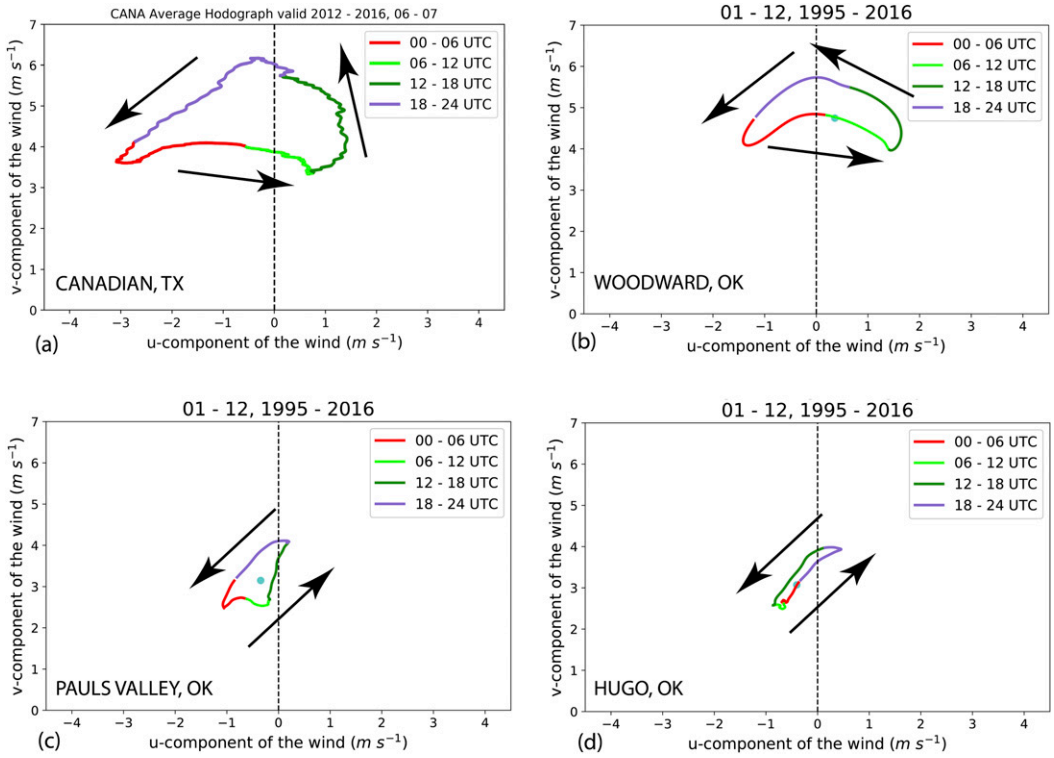

FIG. 6. Time (color coded) dependences of wind hodographs at anemometer level for (a) CAN, TX; (b) WWR, OK; (c) PVL, OK; and (d) HUG, OK. Data in (a) are from the WTM, averaged from June 2012 to July 2016, and data in (b)–(d) are from the OK Mesonet, averaged from 1995 to 2016. The arrows indicate the sense of rotation of the perturbation wind with time. This figure gives more detailed information than that in Fig. 5, but for just four diverse locations. CST and CDT are 6 and 5 h earlier, respectively, than UTC.

found that the removal of the sloping terrain diminished considerably the amplitude of the diurnal oscillation, though it did appear to persist in south Texas (their Fig. 2c), perhaps because the diurnal variation of the eddy coefficient of viscosity is much greater over south Texas than it is to the east, over Florida.

In considering time windows with respect to the annual heating cycle for a more detailed inspection of hodographs of the perturbation wind as a function of time at a constant level, we selected the time period from mid-April through mid-August as a compromise. This includes the period where, in the southern Great Plains, vertical shear strong enough to support supercells can occur, particularly from April to mid-June, as well as a period where conditions are dominated by the summer nocturnal LLJ (e.g., Bonner 1968).

Because heating on a sloping surface has been implicated as a factor in determining the hodographs of the perturbation wind near the ground, composite hodographs were also prepared separately for ''sunny'' days and ''cloudy'' days to see if they differ, and if they do, by how much. Based on the distribution of days having surface radiation exceeding a certain value over the 22-yr period (Fig. 8), sunny days and cloudy days were chosen on the basis of the amount of incoming solar radiation and its relation to the maximum possible by month. The incoming solar radiation was averaged at each mesonet station during the daylight hours, and a threshold was chosen based on the average annual percentage of sunny days. In Oklahoma, the percentage of sunny days each year varies from 60% to 70% (NCDC 2017). The thresholds for sunny and cloudy days varies by month; the threshold chosen for this study for sunny days for each station was approximately 70%, which was not adjusted for each individual station, even though it is likely that there is a difference between stations in eastern and western Oklahoma. It is thought, however, that this simplified analysis is sufficient for our purposes.

Hodographs are shown for Woodward, Oklahoma, and Canadian, Texas, as examples (Fig. 9). On sunny days, the hodographs still have a kidney bean shape, turn in counterclockwise manner with time, and exhibit a maximum variation in the zonal component of the wind of ~3.5–6 m s^{-1}, which is about twice the variation for all days (not shown); furthermore, the meridional wind component oscillates with an amplitude of

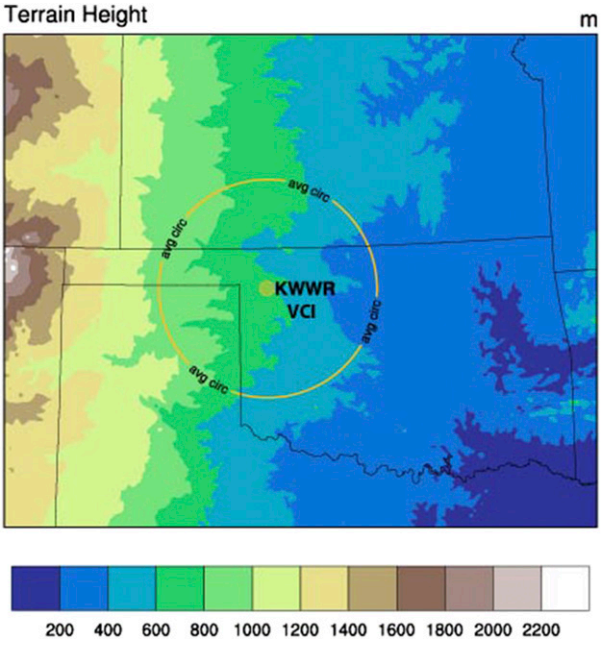

FIG. 7. The terrain height in portions of the southern Great Plains, color coded in m MSL, from the 3-km WRF domain. The location of WWR, OK, is noted, along with a circle of radius 165 km (~1.5° in latitude–longitude) centered at WWR. Diagnostics discussed later were averaged over all model grid points within this circle. The location of the wind profiler at VCI, OK, is also noted.

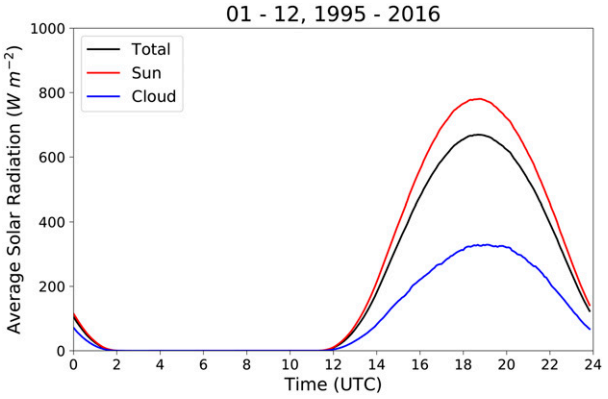

FIG. 8. Average solar radiation (W m^{-2}) as a function of time (UTC; LT is 5 h earlier) at WWR, OK, averaged from 1995 to 2016. The red, blue, and black curves are for sunny, cloudy, and total (all) days, respectively.

approximately 1 m s^{-1}. On cloudy days, however, the perturbation winds are much weaker; the maximum variation in the zonal component of the wind is only ~2 m s^{-1}, and the zonal wind component is easterly. The association of easterly winds with cloudy days is likely a consequence of easterly upslope winds in the western plains, to the rear of surface cold fronts, with low clouds.

It therefore appears as if the NARR analyses (and the GCM simulations), which show a clockwise turning of the perturbation-wind hodographs with time, differ from the observations of counterclockwise turning with time in the Oklahoma and West Texas Mesonet datasets. We propose that this apparent discrepancy is because the wind observations are made at different altitudes. To test this assertion, we consider wind data averaged over a 5-yr period from the now-defunct NOAA WPDN at Vici, Oklahoma, which is just ~35 km south-southeast of Woodward (see Fig. 7). The hodograph at 500 m turns in a clockwise manner with time, like the NARR and GCM data of Jiang et al. (2007), while the wind at 10 m AGL generally turns in a counterclockwise manner with time (Fig. 10), like the mesonet data. In addition, wind data from an instrumented tower in the northern part of Oklahoma City, averaged over a 1-yr period (Crawford and Hudson 1973, their Fig. 5; Fig. 11), also display a clockwise turning of the wind with time above anemometer level (usually taken to be 10 m AGL). At anemometer level, but 250 ft (i.e., <100 m) northwest of the base of the tower because the tower base was located in a shallow gully, the magnitude of the perturbation wind was much less, and the wind turned in a counterclockwise manner with time from just after 0000 CST to sometime after 1200 CST[2] (UTC is 6 and 5 h later, respectively, than CST and CDT); however, it traced out a highly elliptical, kidney-shaped hodograph, similar to the ones shown in Figs. 6a and 6b. It therefore appears as if winds in parts of the southern plains behave quite differently at anemometer level than they do at higher altitudes in the boundary layer. To understand why this is so, we analyzed data from numerical simulations, for which one has most of the variables needed to diagnose the forces driving the change in the winds with time. The authors are not aware of any other study that focuses on the turning of the winds with time at anemometer level in the Great Plains.

4. Numerical model analyses

Because individual case studies would be very difficult, owing to the difficulty in finding real cases under pristine, quiescent conditions, we chose to look at the time average of many WRF ensemble forecasts, which should filter out transient, mobile disturbances. Because running a model for many days, especially one with a number of ensemble members, is computationally intense and expensive, we initially used a set of data that

[2] The sense of the turning of the winds with time at anemometer level was not discussed in Crawford and Hudson (1973), probably because it is difficult to discern at longitudes as far east as those of central Oklahoma (our Fig. 5).

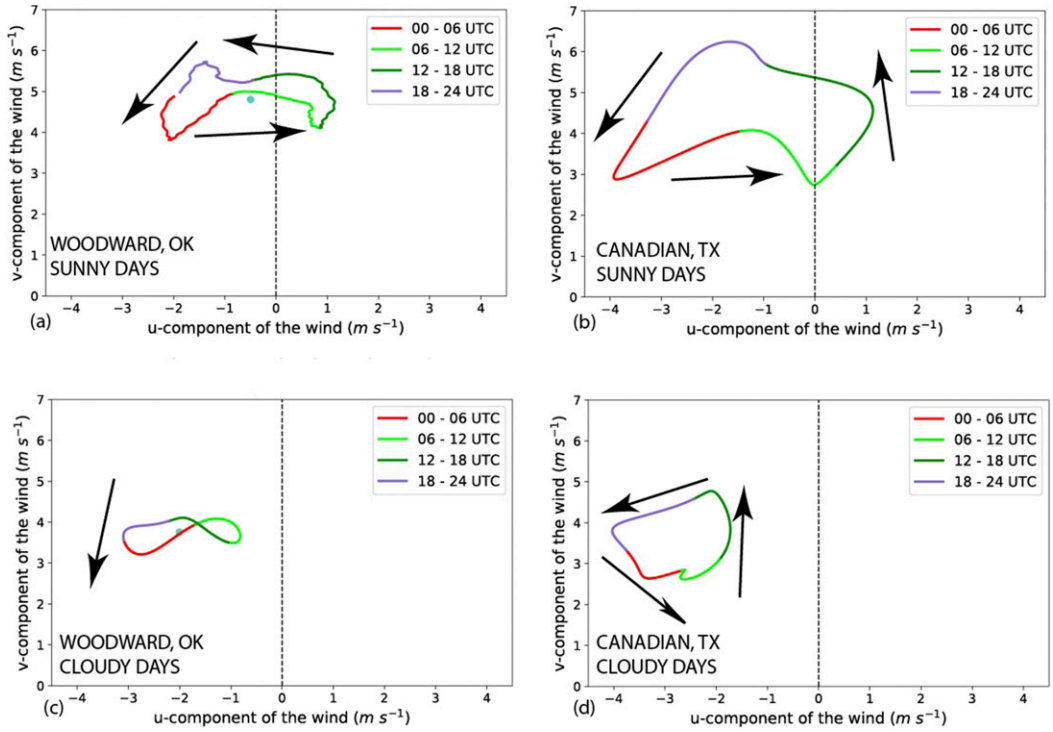

FIG. 9. As in Fig. 6, but just for the warm season (May–August) at WWR, OK, on (a) sunny and (c) cloudy days, averaged from 1995 to 2016, and for CAN, TX, on (b) sunny and (d) cloudy days, averaged from 2012 to 2016.

was already available. This dataset was one from the earlier-described NCAR ensemble for 12–35-h forecasts initialized at 0000 UTC from 15 April to 15 August 2016. As such, it is not valid for the same time window used earlier for the observations. Still, averaging the 10-m diagnostic winds over this period for each time of day produces similar results to those shown in the observational analysis (cf. Figs. 12, 5). Perturbation winds rotate counterclockwise in the southern Great Plains through the diurnal cycle, particularly in regions where the terrain is sloping with increasing elevation to the west.

In a hodograph showing the lowest and third-lowest model levels from a grid point near Woodward, Oklahoma, the diurnally averaged winds couple around midday, follow closely during the early and mid-afternoon with slightly stronger winds aloft, but diverge sharply during the late afternoon and evening hours (Fig. 13). The strongest westerly component of the wind at low levels is found at ~600 m–1.2 km AGL at 0900–1200 UTC (0400–0700 CDT), while the strongest easterly component is found at 0300 UTC (2200 CDT) just under 200 m AGL (Fig. 14a). The strongest southerly component is found at 0600 UTC (0100 CDT) near 600 m AGL (Fig. 14b), consistent with LLJ climatology.

Using the retrospective forecasts, diagnostic quantities were computed as spatial averages of data from all grid points within 165 km, or ~1.5°, of Woodward in order to filter out noise in the simulations related to flow over local topography. Again, Woodward was chosen because it lies in the region where the amplitude of the diurnal oscillation in the wind is relatively large. Our method of diagnosis is similar to that of Bell and Bosart (1988), Bluestein and Crawford (1997), and Moisseeva and Steyn (2014), who estimated forces driving horizontal motions at the surface. In the case of the two former studies, only observational wind and pressure data at the surface were used. The effects of vertical mixing were computed as a residual, among the parcel acceleration, Coriolis, PGF, and friction forces (by friction, we mean the sum of vertical mixing and surface drag; horizontal mixing and curvature terms are found to be small and are, therefore, neglected in this analysis) and a parameterized surface drag (see Figs. 17, 18). The former observational analyses were especially subject to errors in the estimate of the PGF because pressure measurements were made on a sloping surface, as well as to errors in the wind-related quantities, for which a linear variation between adjacent stations was assumed. In the case of the latter, data from numerical simulations were used so that all forces could be computed directly.

a. Hodographs at constant level averaged over time

The time-averaged hodograph near Woodward at the first level in the WRF Model, which is at 28 m AGL, exhibits a general counterclockwise turning with time,

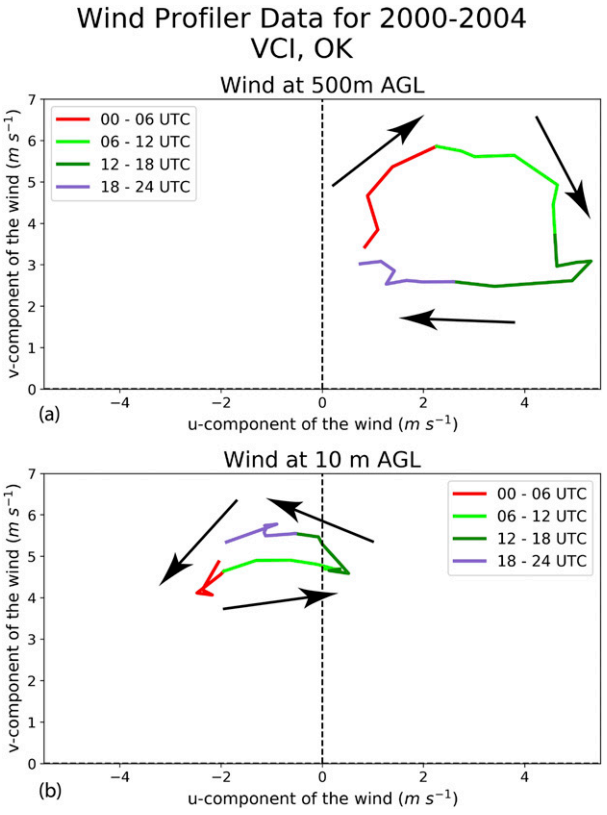

FIG. 10. As in Fig. 6, but for wind profiler data at VCI, OK (see Fig. 5), at (a) 500 and (b) 10 m AGL, averaged from 2000 to 2004.

especially from ~1300 to ~0400 CDT, while the hodograph at the third from the bottom level, which is at 184 m AGL, exhibits a clockwise turning with time (Fig. 13). Thus, the hodographs near anemometer level and the hodographs in the boundary layer based on WRF forecasts averaged over time are qualitatively similar to the observations. It is, therefore, hypothesized that the physical processes responsible for the anomalous turning with time of the hodographs at anemometer level in real data are correctly represented in the model forecasts and that a diagnosis of the model forecasts can be used to determine the causes of the anomalous turning. Because the hodograph at the model level between the lowest and third-lowest levels tended to cross over itself along a northwest to southeast direction, the discussion that follows examines hodographs at the lowest and third-lowest model levels.

The hodographs at both anemometer level and in the boundary layer exhibit a diurnal oscillation, with a large component in the upslope direction (to the west) during the day and in the downslope direction (to the east) at night. Both model-forecast hodographs have a kidney bean shape like the observed hodographs. The main differences in the model hodographs occur during the late afternoon and early evening. At 184 m AGL, the winds veer sharply around 2200, while at the same time, the winds at the anemometer level back sharply. Furthermore, from about 1600 to 2200, the winds aloft diverge from the winds below somewhat so that the shear in the lowest ~150 m (from 28 to 184 m AGL) increases from about 0.6 to 3.5 m s^{-1} over the lowest 150 m (Fig. 13), or by a factor of 6 from 1600 to 2200 and by a factor of 9 from 1300 to 2200. In addition, the surface wind backs from 1300 to 2200, resulting in a decrease in the westerly component of the wind by about 2 m s^{-1}, so that the surface to ~6-km shear increases by about 2 m s^{-1} over 6 km, assuming that the 500-hPa wind (~6 km) does not change during the same time period and is from the west. The reader is reminded that while the increase in shear suggested by the model is small, it represents an average over many forecasts, including those for cloudy days. If the atmosphere were quiescent on an individual day, and if the exact initial conditions were specified, the increases in shear could be much greater.

b. *Diagnosis of the forces responsible for the time changes in the wind*

To find out why the hodographs behave the way they do, we consider the horizontal equation of motion:

$$D\mathbf{V}/Dt = \mathrm{CoF} + \mathrm{PGF} + \partial\boldsymbol{\tau}/\partial z, \tag{1}$$

where $\mathbf{V}$ is the horizontal wind vector, CoF is the acceleration induced by the Coriolis force, PGF is the acceleration induced by the horizontal pressure gradient force, and $\partial\boldsymbol{\tau}/\partial z$ is the vertical eddy stress term (the horizontal eddy stress term is considered negligible). In the boundary layer, the stress can be approximated as

$$\boldsymbol{\tau} = \mu\partial\mathbf{V}/\partial z, \tag{2}$$

where μ depends on the static stability and vertical shear, among other things. Furthermore, in the surface friction layer, which includes anemometer level,

$$\boldsymbol{\tau} = \rho C_D|\mathbf{V}_0|\mathbf{V}_0. \tag{3}$$

As in Bell and Bosart (1988) and Bluestein and Crawford (1997), we may interpret $\partial\boldsymbol{\tau}/\partial z$, the friction term, as having a part due to vertical mixing and a part due to "surface" drag; the latter always contributes to a reduction in wind speed, while the former increases/decreases and turns the wind depending on how the vertical shear vector is directed and how strong it is.

In the Eulerian reference frame, (1) becomes

$$\partial\mathbf{V}/\partial t = -\mathbf{V}\cdot\nabla\mathbf{V} + \mathrm{CoF} + \mathrm{PGF} + \partial\boldsymbol{\tau}/\partial z, \tag{4}$$

where $-\mathbf{V}\cdot\nabla\mathbf{V}$ is the acceleration due to the advection (both horizontal and vertical) of momentum. [In Bell

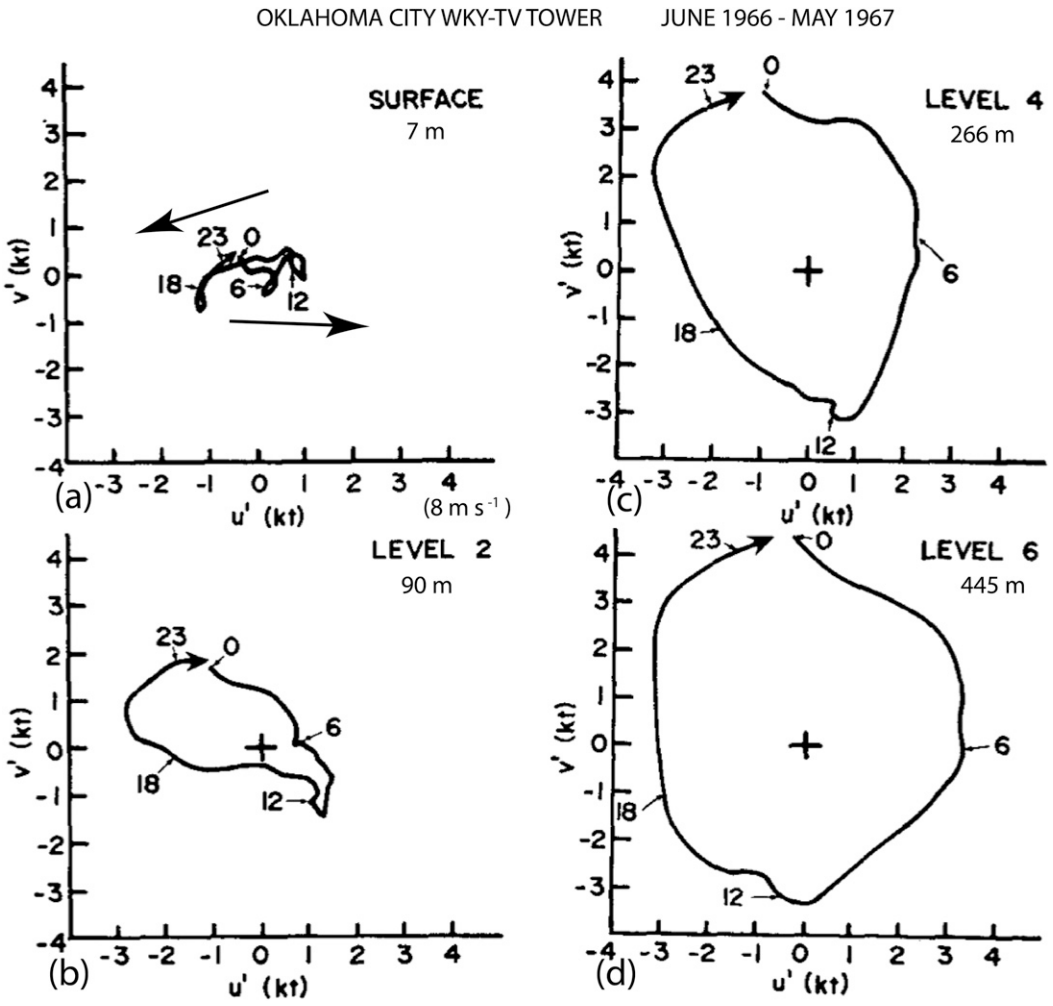

FIG. 11. Time dependences of perturbation-wind hodographs on the instrumented WKY-TV tower in northern Oklahoma City, averaged from June 1966 to May 1967, at (a) 7, (b) 90, (c) 266, and (d) 445 m AGL. The arrows indicate the sense of rotation of the perturbation wind with time [adapted from Crawford and Hudson (1973), their Fig. 5].

and Bosart (1988) and Bluestein and Crawford (1997), $\partial\tau/\partial z$ was calculated as a residual in (4).] The advection term is positive when the wind speed decreases downstream, and vice versa. So, upstream and downstream from the LLJ, this term is negative and positive, respectively.

The accelerations averaged within 165 km (~1.5°) of Woodward (see Fig. 7) due to each of the four terms in (4) and the parcel acceleration [the left-hand side of (1)] in the zonal (x) and meridional (y) directions are shown in Figs. 15a and 15b, respectively, as a function of local time at the lowest level (anemometer level; thick lines) and just above (thin lines). At 1700, the westward-directed component of the PGF at both levels is greatest and diminishes steadily until ~0700. At 1300–1400, the meridional component of the friction term at the lowest level (Fig. 15b) decreases, that is, becomes more strongly directed to the south, or roughly opposite to that of the wind; the meridional component of the wind at anemometer level decreases in response to this relatively sudden burst of intensity, which reaches its greatest level around 1900. (Fig. 16b). Horizontal advection is negligible in the zonal direction but is slightly negative in the meridional direction, perhaps indicative of Woodward's location being upstream from the LLJ.

The u component of the wind at both anemometer level and in the boundary layer (184 m AGL) above reaches its maximum from the east around 2100–2200, then becomes less easterly with time and vanishes

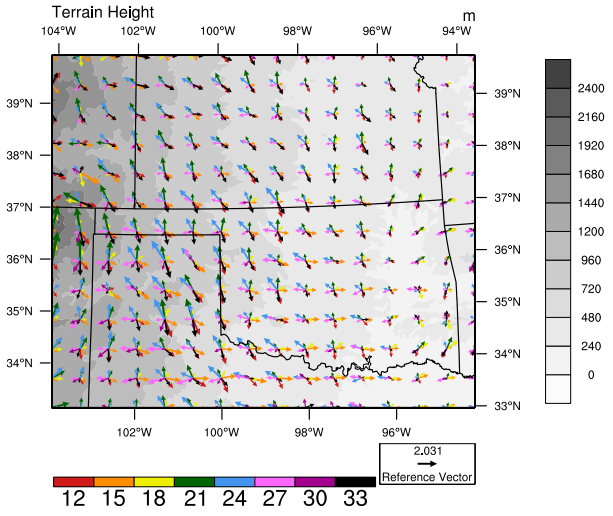

FIG. 12. As in Fig. 5, but from 12- to 33-h averaged perturbation 10-m diagnostic winds from WRF ensemble forecasts initialized from 0000 UTC 15 Apr to 15 Aug 2016 at selected grid points regionally, color coded differently, as shown in hours from the initial time of 0000 UTC. All times are equivalent to the time in UTC, except for times at and beyond 24 h, which are shown in UTC only in parentheses. Terrain height (m MSL) is shown in grayscale.

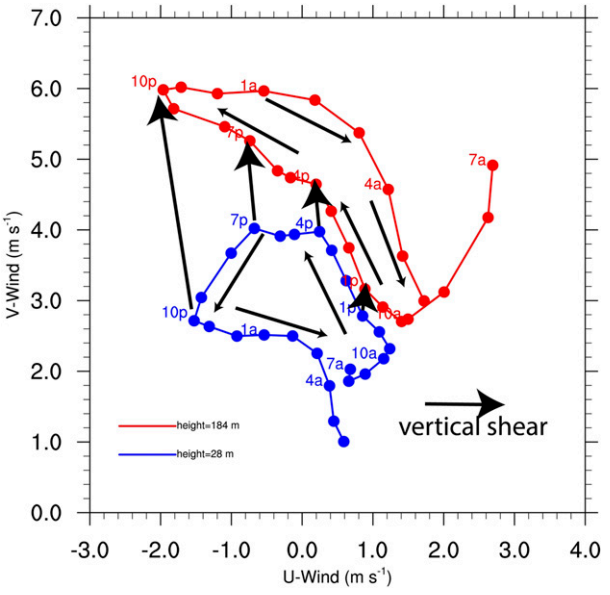

FIG. 13. Time dependence (CDT; LT) of wind hodographs from WRF ensemble runs at WWR, OK, during the warm season, averaged from 12- to 35-h forecasts initialized from 0000 UTC 15 Apr to15 Aug 2016 at the lowest and third-lowest model levels with average heights of 28 (blue) and 184 m AGL (red), respectively. Arrows with small heads indicate the sense of the rotation of the perturbation winds with time. Black arrows with large heads indicate vertical shear between 28 and 184 m AGL; the magnitude of the shear is proportional to the lengths of the vectors. The shear, which is approximately from the south-southeast, increases markedly from 1300 to 2200.

around 0300, becoming slightly westerly at anemometer level until ~1000 (Fig. 16a). On the other hand, the v component of the wind behaves differently (Fig. 16b): the southerly component of the wind continues to increase after 1600 at 184 m AGL, while the southerly component of the wind decreases at anemometer level after 1900. It continues to decrease until around 0700, while the southerly component of the wind at 184 m AGL does not begin to decrease until after ~2300. It appears as if the southerly component of the wind at anemometer level decreases after 1900 as a result of the increase in the negative y component of the friction term, while the v component of the wind continues to increase at 184 m AGL, where there is no substantial increase in the magnitude of the negative friction term at 1900 (Fig. 15b), as there is at anemometer level.

To gain more insight into the forces responsible for turning the hodograph at anemometer level to the left rather than to the right, we now consider vector force diagrams at four selected times (Figs. 17, 18): 1500, 1900, 2200, and 0300.

At 1500, wind shear vectors (which are tangent to the hodographs) at both anemometer level and aloft, in the boundary layer, point in approximately the same direction, north-northwest (Fig. 13), while the parcel-acceleration vectors at both anemometer level and aloft also point north-northwest (Figs. 17a,c).

At 1900, the directions of the hodographs begin to diverge from each other (Fig. 13), while the parcel-acceleration vector aloft points to the northwest, and the parcel-acceleration vector at anemometer level points west-southwest (Figs. 17b,d).

At 2200, the hodograph at anemometer level turns to the left, and the hodograph aloft turns to the right (Fig. 13), while the parcel-acceleration vectors point northeast aloft and east at anemometer level (Figs. 18a,c).

At 0300, wind shear vectors at both levels point in the same direction, which is southeast (Fig. 13), while the parcel acceleration vectors at both anemometer level and aloft also point southeast (Figs. 18b,d).

At 1500 (Figs. 17a,c), PGF largely drives $D\mathbf{V}/Dt$ at both anemometer level and above, overcoming the CoF and $\partial\boldsymbol{\tau}/\partial z$, which have components in the opposite direction. The CoF also has a component that forces air to the right of PGF. There is a component of $\partial\boldsymbol{\tau}/\partial z$ that acts in the direction opposite to the wind and also to the right of the wind. The former represents surface drag, and the latter represents the mixing down of westerly momentum from aloft.

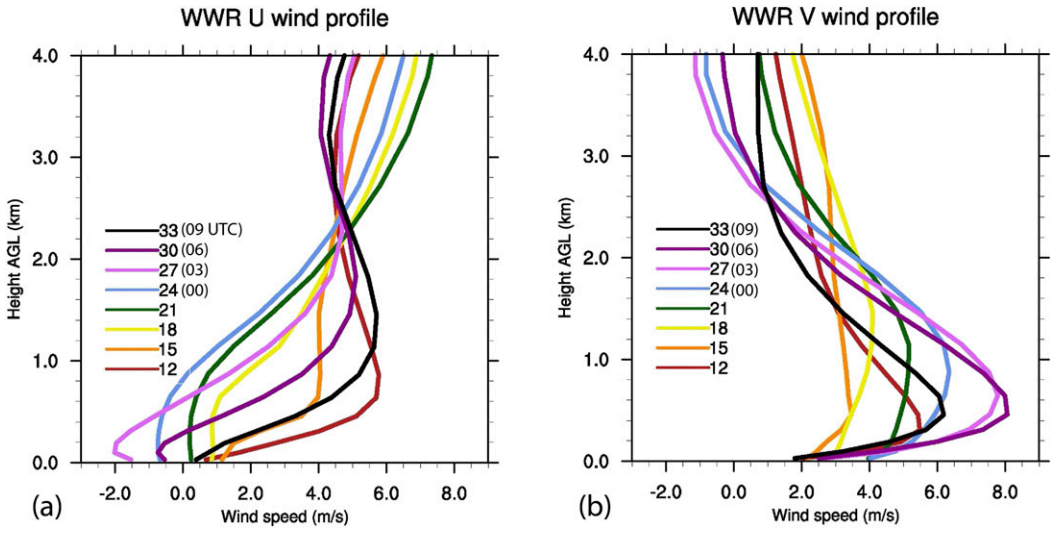

FIG. 14. Variation of the (a) u component of the wind and (b) v component of the wind (abscissa) as a function of height (ordinate) and time (color coded by forecast hour) from 12- to 33-h WRF ensemble forecasts initialized from 0000 UTC 15 Apr to15 Aug 2016. The time in UTC is shown in parentheses; prior to 0000 UTC, the time shown is also equivalent to the time in UTC.

At 1900 (Figs. 17b,d), PGF still largely drives $D\mathbf{V}/Dt$ at anemometer level, but $\partial\boldsymbol{\tau}/\partial z$ is now oriented more in the direction opposite to the wind and much less to the right of the wind, thus allowing $D\mathbf{V}/Dt$ to point now approximately to the left of the wind, in the direction nearly opposite to that of CoF. At 184 m AGL, $\partial\boldsymbol{\tau}/\partial z$ also acts less to the right of the wind, and $D\mathbf{V}/Dt$ has a component in the same direction as $\mathbf{V}$. At both levels, $\partial\boldsymbol{\tau}/\partial z$ acts less to the right of the wind as a consequence of a decrease in vertical mixing of westerly momentum from aloft as the boundary layer stabilizes with the loss of strong surface heating.

At 2200 (Figs. 18a,c), PGF has decreased so much at both levels that the sum of CoF and $\partial\boldsymbol{\tau}/\partial z$ overwhelms it, so $D\mathbf{V}/Dt$ now has a component in the direction opposite to the wind at anemometer level and to the right and 45° of the wind at 184 m AGL, as in an inertial oscillation. At 2200, advection of momentum at 184 m AGL is no longer relatively small, but is comparable to the next-stronger acceleration, $\partial\boldsymbol{\tau}/\partial z$. This increase in the importance of advection might be related to the increase in the v component of the wind at night in the boundary layer (Fig. 16b), especially to the north of Woodward (not shown). It is not as strong at anemometer level. Overall, air accelerates to the northeast at 184 m AGL, but much more to the east at anemometer level, thus accounting for the clockwise turning aloft and the counterclockwise turning at anemometer level.

At 0300 (Figs. 18b,d), except for advection at anemometer level, which is negligible, all accelerations are relatively small and of the same order of magnitude. The parcel acceleration is to the southwest at both levels.

5. Conclusions and discussion

On the basis of both observations and model forecasts, it was found that the hodographs for the perturbation wind at anemometer level in the western portions of the southern plains (the Texas Panhandle and western Oklahoma) turn in an anomalous counterclockwise direction with time, the opposite of what is found above in the boundary layer, especially above ~150–200 m AGL. In most literature on the winds in the southern plains, it has been shown or assumed that the perturbation winds turn in a clockwise manner with time in a quiescent atmosphere.

The amplitude of the diurnal variation in the zonal component of the wind is greatest for stations in the western portion of the plains, where the terrain gradient, mostly directed to the west, is the greatest. The amplitude is greatest for sunny days during the warm season, when the surface heating is greatest and can account for an increase in the easterly component of the wind of 6 m s^{-1} over the diurnal heating cycle. This diurnal oscillation is responsible for changes in vertical shear in the lowest 150 m and also between 0 and 6 km, if the 6-km wind remains unchanged. An increase in vertical shear of ~6 m s^{-1} over the lowest 6 km may be enough to affect the

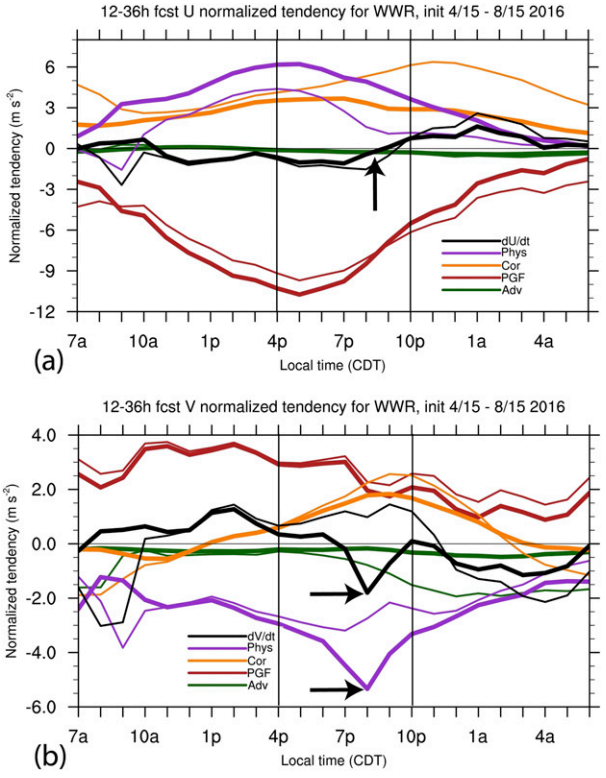

FIG. 15. Individual horizontal acceleration terms in (4), normalized by the magnitude of the Coriolis parameter, as a function of time (CDT; LT) in the (a) x (zonal) direction and the (b) y (meridional) direction. Data are from the WRF ensemble forecast runs, averaged during the warm season, for 12–35-h forecasts initialized from 0000 UTC 15 Apr to 15 Aug 2016. The thick (thin) curve is valid for the lowest model level near 28 m AGL (third-lowest model level near 184 m AGL). Note that the range in acceleration terms in (a) is much larger than in (b). The black, purple, orange, red, and green lines represent the parcel acceleration, vertical component of the stress (boundary layer physics), acceleration associated with the Coriolis force, acceleration associated with the PGF, and advection of momentum, respectively. Vertical lines are shown at 1600 and 2200 to highlight the late afternoon and evening boundary layer transition. The arrow in (a) shows when Du/Dt transitions from negative to positive near 28 m AGL, that is, when Ekman balance in the x direction is disturbed during the evening. Arrows in (b) indicate when Dv/Dt is most negative (directed toward the south), at around 2000 (black curve), and when the vertical derivative of the meridional component of the stress is most negative (directed toward the south), also at 2000.

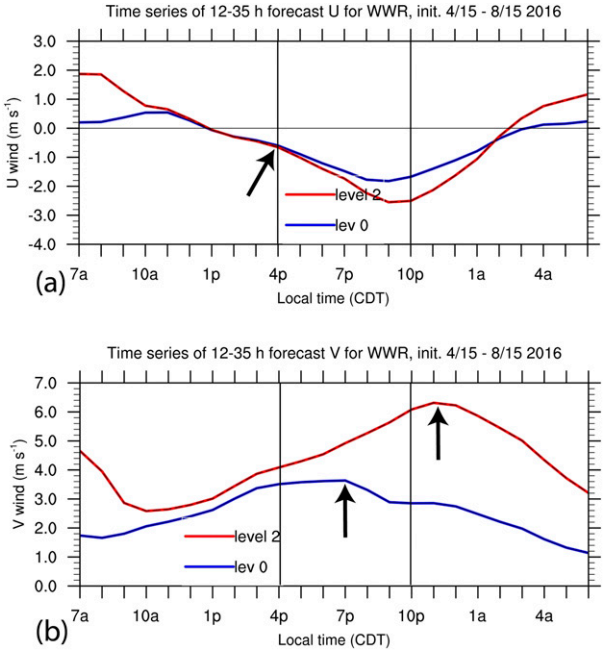

FIG. 16. As in Fig. 15, but for just (a) the u (zonal) component of the wind and (b) the v (meridional) component of the wind. The blue (red) lines show time series at 28 (184) m AGL. The arrow in (a) indicates when the zonal components of the wind during late afternoon begin to differ from each other. The arrows in (b) show how the v component of the wind at 28 m begins to decrease shortly after 1900, while the v component of the wind at 184 m continues to increase and does not begin to decrease until much later, around 2300.

mode of convection. For example, if the shear increases from 15 m s^{-1} over the lowest 6 km, which is supportive of multicell convection when there is sufficient CAPE, to 20 m s^{-1} over the lowest 6 km, then the shear is supportive of supercell convection. Although the shear in the lowest 150 m also increases, it is not clear if it is sufficient to change the environment enough so that it becomes much more conducive for tornadogenesis.[3]

Anomalous counterclockwise turning of the perturbation wind with time at the surface was noted by Mass (1982, his Fig. 12) in western Washington, on the western side of Puget Sound and at Port Angeles, on the southern side of the Strait of Juan de Fuca. Mass (1982) cited a U.S. Army Signal Corps report on mountain and valley winds by Hawkes (1945), who noted the same counterclockwise turning on the left side of terrain that slopes down a valley. Because Puget Sound is like a valley that slopes downward to the north, Mass (1982, p. 181) attributed the counterclockwise turning to a "dominating 'valley' wind that 'overcame' the clockwise turning with time induced by the Coriolis force." In this case, however, the terrain is much more steeply sloped than the gentler slopes over the western portion of the plains. In addition, the sea–land breeze circulations

[3] The 0–1-km storm-relative helicity (SRH) during the afternoon was ~18 m^2 s^{-2}, increased to ~24 m^2 s^{-2} by evening, and reached ~50 m^2 s^{-2} by late evening. It is thought that an SRH of ≥100 m^2 s^{-2} is associated with an enhanced tornado risk (Rasmussen and Blanchard 1998).

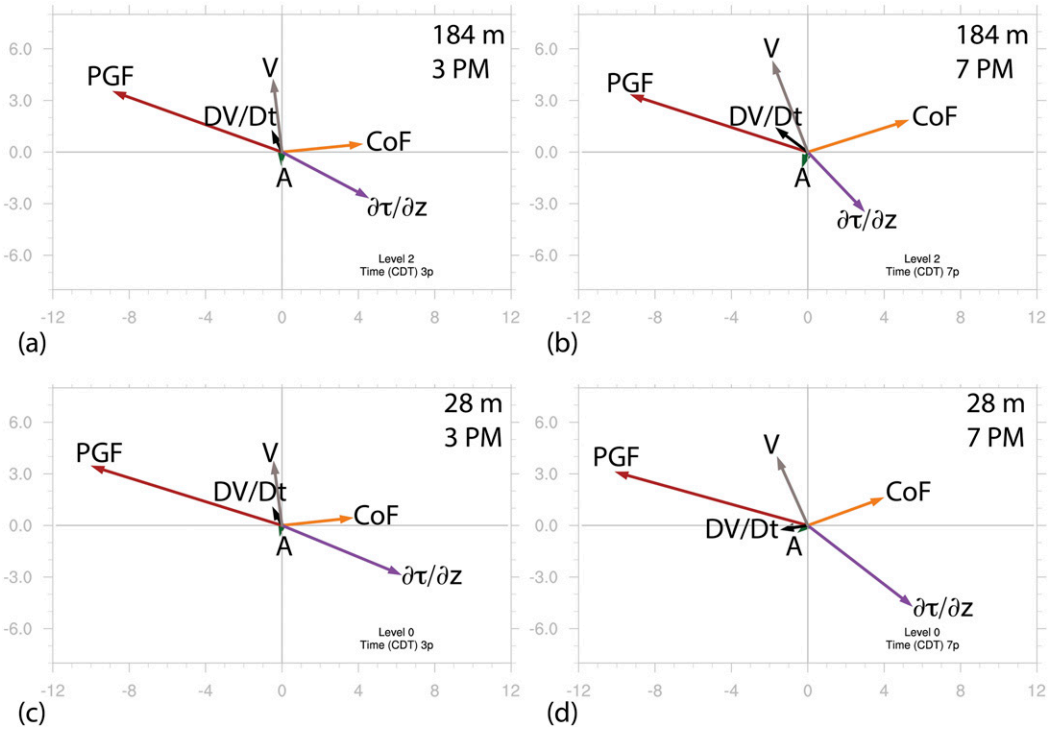

FIG. 17. Horizontal vectors indicating the terms in (4) and the wind as a function of time and height, from the WRF ensemble runs from 15 Apr to 15 Aug 2016. (a) 184 m AGL at 1500 (CDT; LT); (b) 28 m AGL at 1500; (c) 184 m AGL at 1900; and (d) 28 m AGL at 1900. Parameters **V,** $D\mathbf{V}/Dt$, PGF, CoF, $\partial\boldsymbol{\tau}/\partial z$, and **A** represent the wind, parcel acceleration, acceleration associated with the Coriolis force, the vertical component of the stress, and the advection of momentum, respectively. The acceleration vectors are scaled by the Coriolis parameter ($\mathrm{m\,s^{-2}}$), and the wind vectors are given in $\mathrm{m\,s^{-1}}$.

could play a role. Moisseeva and Steyn (2014, see their Fig. 2) also noted anomalous counterclockwise turning of the perturbation wind with time at some locations on the northwestern coast of the island of Sardinia in the Mediterranean and in an idealized WRF simulation over an isolated island with orography. They attributed the anomalous turning to diurnal variations in terrain-related thermal forcing. Van de Wiel et al. (2010) have documented what they termed a "backward inertial oscillation" in a 7-night composite of data from an observatory in the Netherlands. This finding, however, involved only the surface wind speed and did not involve any counterclockwise turning of the perturbation surface wind vector. Furthermore, the terrain does not slope in the Netherlands, as it does in the central United States.

The anomalous turning of the winds, especially in the late afternoon and evening, based on diagnoses of data from WRF forecasts of the forces acting at anemometer level and aloft within the boundary layer, appears to be caused by a spike in a negative vertical derivative of stress in the meridional direction, which peaks at 2000. (Fig. 15b). After 1600, the thermally directed upslope component of the PGF weakens, and vertical mixing of momentum from aloft decreases. These factors result in a turning of $\partial\boldsymbol{\tau}/\partial z$ in a clockwise direction, less to the right of the wind and more in the direction opposite to the wind. By 1900, vertical mixing has weakened considerably aloft, but at anemometer level, the stress due to the southerly wind persists. Because the effect on parcel acceleration by $\partial\boldsymbol{\tau}/\partial z$ above anemometer level is

$$\partial\boldsymbol{\tau}/\partial z \approx [\boldsymbol{\tau}(\text{in the boundary layer at} \sim 200\,\text{m}) - \boldsymbol{\tau}(\text{anemometer level})]/200\,\text{m}, \quad (5)$$

where $\boldsymbol{\tau}$ (in the boundary layer, at ~200 m) $= \mu\partial\mathbf{V}/\partial z$. The latter quantity decreases as μ decreases when the boundary layer stabilizes as the sun goes down and/or when $\mu\partial\mathbf{V}/\partial z$ becomes approximately constant with height. If, for example, the vertical shear vanishes above the boundary layer (e.g., Grant 1997; Bell and Bosart 1988),

$$\partial\boldsymbol{\tau}/\partial z(\text{above anemometer level}) \approx -\boldsymbol{\tau}(\text{anemometer level})/200\,\text{m} = -\rho\, C_D|\mathbf{V}_0|\mathbf{V}_0. \quad (6)$$

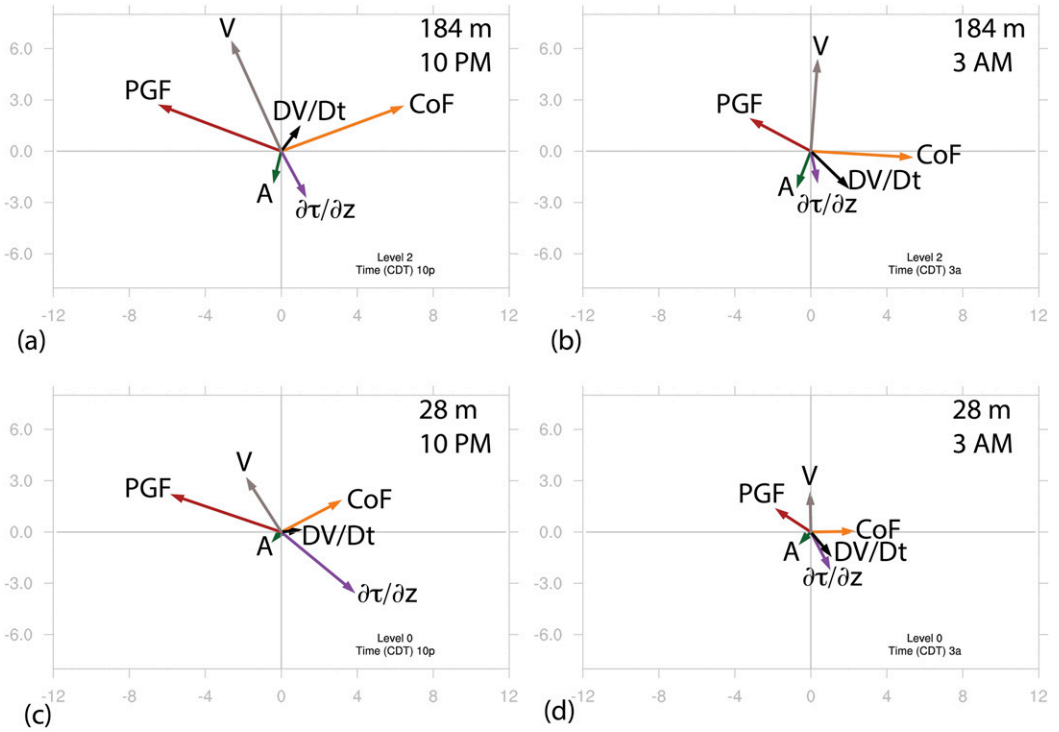

FIG. 18. As in Fig. 17, but for later time periods: 2200 (27-h forecast) and 0300 (32-h forecast).

Mahrt (1981, p. 329), on the other hand, found from observations in Australia that during the early evening, $|\partial\boldsymbol{\tau}/\partial z|$ in the lowest 200 m increases because "the influence of decreasing boundary layer depth exceeds the effect of decreasing surface stress," which leads to "temporary deceleration and rotation of the low-level wind vector toward low pressure and, thus, increases the ageostrophic flow."

Because the stress at anemometer level is given by (3), that is, is positive in the direction of the wind, the meridional component of $\partial\boldsymbol{\tau}/\partial z$ decreases when the magnitude of the meridional component of $\boldsymbol{\tau}$ (in the boundary layer, at ~200 m) decreases. Aloft, on the other hand, $\partial\boldsymbol{\tau}/\partial z$ decreases in magnitude, so the sum of it and CoF and $\partial\boldsymbol{\tau}/\partial z$ and advection is directed more in the opposite direction to PGF, and the resultant parcel acceleration acts to the right of the wind at anemometer level.

Direct diagnoses of the stress at anemometer level and aloft were not possible using the WRF simulations, so the inferences noted above are based on evidence of the direction and magnitude of changes in $\partial\boldsymbol{\tau}/\partial z$ as a function of time of day and must, therefore, be viewed as tentative in a quantitative sense but accurate in a qualitative sense.

In the future, detailed measurements of the perturbation wind as a function of time of day need to be made in the real atmosphere in the plains over a period of many months or years using instruments such as sodars, which can measure the wind as a function of time with high spatial resolution in the vertical. Doppler sodars (Busse and Knupp 2012) can measure winds as low as 30 m AGL but with a range only up to ~200 m under clear-air conditions (P. Klein 2017, personal communication). Also, model simulations need to be made in which the stresses can be retrieved to illuminate further how and why $\partial\boldsymbol{\tau}/\partial z$ changes after 1600 CDT.

Acknowledgments. This study was supported by NSF Grant AGS-1560945 and by NOAA Grant NA15OAR4590191 to Glen Romine at UCAR/NCAR. Much of the work was done at the Mesoscale Microscale Meteorology (MMM) Division at NCAR. The first author thanks NCAR for its support with a Faculty Fellowship during his sabbatical leave and for hosting a summer visit. We also are grateful for useful discussions with Peggy LeMone (NCAR), Morris Weisman (NCAR), Alan Shapiro (University of Oklahoma), and Cliff Mass (University of Washington). The Oklahoma Climatological Survey at the University of Oklahoma provided Oklahoma Mesonet data, the National Wind Institute at Texas Tech University provided West Texas Mesonet data, and NOAA provided WPDN data; Paul Neiman (NOAA/ESRL) provided information about the

surface instrumentation at profiler sites. We also acknowledge high-performance computing support from Yellowstone (ark:/85065/d7wd3xhc), provided by NCAR's Computational and Information Systems Laboratory, sponsored by the National Science Foundation.

REFERENCES

Bell, G. D., and L. F. Bosart, 1988: Appalachian cold-air damming. *Mon. Wea. Rev.*, **116**, 137–161, https://doi.org/10.1175/1520-0493(1988)116<0137:ACAD>2.0.CO;2.

Blackadar, A. K., 1957: Boundary layer wind maxima and their significance for the growth of nocturnal inversions. *Bull. Amer. Meteor. Soc.*, **38**, 283–290.

Bluestein, H. B., 1992: *Principles of Kinematics and Dynamics.* Vol. 1, *Synoptic-Dynamic Meteorology in Midlatitudes,* Oxford University Press, 448 pp.

——, 2009: The formation and early evolution of the Greensburg, Kansas, tornadic supercell on 4 May 2007. *Wea. Forecasting*, **24**, 899–920, https://doi.org/10.1175/2009WAF2222206.1.

——, 2013: *Severe Convective Storms and Tornadoes: Observations and Dynamics.* Springer, 456 pp., https://doi.org/10.1007/978-3-642-05381-8.

——, and D. A. Speheger, 1995: The dynamics of an upper-level trough in the baroclinic westerlies: Analysis based upon data from a wind profiler network. *Mon. Wea. Rev.*, **123**, 2369–2383, https://doi.org/10.1175/1520-0493(1995)123<2369:TDOAUL>2.0.CO;2.

——, and T. M. Crawford, 1997: Mesoscale dynamics of the near-dryline environment: Analysis of data from COPS-91. *Mon. Wea. Rev.*, **125**, 2161–2175, https://doi.org/10.1175/1520-0493(1997)125<2161:MDOTND>2.0.CO;2.

——, and A. L. Pazmany, 2000: Observations of tornadoes and other convective phenomena with a mobile, 3-mm wavelength, Doppler radar: The spring 1999 field experiment. *Bull. Amer. Meteor. Soc.*, **81**, 2939–2951, https://doi.org/10.1175/1520-0477(2000)081<2939:OOTAOC>2.3.CO;2.

Bonner, W. D., 1968: Climatology of the low level jet. *Mon. Wea. Rev.*, **96**, 833–850, https://doi.org/10.1175/1520-0493(1968)096<0833:COTLLJ>2.0.CO;2.

——, and J. Paegle, 1970: Diurnal variations in boundary layer winds over the south-central United States in summer. *Mon. Wea. Rev.*, **98**, 735–744, https://doi.org/10.1175/1520-0493(1970)098<0735:DVIBLW>2.3.CO;2.

Bosart, L. F., A. Seimon, K. D. LaPenta, and M. J. Dickinson, 2006: Supercell tornadogenesis over complex terrain: The Great Barrington, Massachusetts, tornado on 29 May 1995. *Wea. Forecasting*, **21**, 897–922, https://doi.org/10.1175/WAF957.1.

Brock, F. V., K. Crawford, R. Elliott, G. Cuperus, S. Stadler, H. Johnson, and M. Eilts, 1995: The Oklahoma Mesonet: A technical overview. *J. Atmos. Oceanic Technol.*, **12**, 5–19, https://doi.org/10.1175/1520-0426(1995)012<0005:TOMATO>2.0.CO;2.

Brooks, H. E., J. W. Lee, and J. P. Craven, 2003: The spatial distribution of severe thunderstorm and tornado environments from global reanalysis data. *Atmos. Res.*, **67–68**, 73–94, https://doi.org/10.1016/S0169-8095(03)00045-0.

Busse, J., and K. Knupp, 2012: Observed characteristics of the afternoon–evening boundary layer transition based on sodar and surface wind data. *J. Appl. Meteor. Climatol.*, **51**, 571–582, https://doi.org/10.1175/2011JAMC2607.1.

Chen, F., and J. Dudhia, 2001: Coupling an advanced land surface–hydrology model with the Penn State–NCAR MM5 modeling system. Part I: Model implementation and sensitivity. *Mon. Wea. Rev.*, **129**, 569–585, https://doi.org/10.1175/1520-0493(2001)129<0569:CAALSH>2.0.CO;2.

Crawford, K. C., and H. R. Hudson, 1973: The diurnal wind variation in the lowest 1500 ft in central Oklahoma: June 1966–May 1967. *J. Appl. Meteor.*, **12**, 127–132, https://doi.org/10.1175/1520-0450(1973)012<0127:TDWVIT>2.0.CO;2.

Doviak, R. J., and D. S. Zrnić, 1984: *Doppler Radar and Weather Observations.* Academic Press, 458 pp.

Dowell, D. C., and H. B. Bluestein, 1997: The Arcadia, Oklahoma, storm of 17 May 1981: Analysis of a supercell during tornadogenesis. *Mon. Wea. Rev.*, **125**, 2562–2582, https://doi.org/10.1175/1520-0493(1997)125<2562:TAOSOM>2.0.CO;2.

Du, Y., and R. Rotunno, 2014: A simple analytical model of the nocturnal low-level jet over the Great Plains of the United States. *J. Atmos. Sci.*, **71**, 3674–3683, https://doi.org/10.1175/JAS-D-14-0060.1.

Grant, A. L. M., 1997: An observational study of the evening transition boundary-layer. *Quart. J. Roy. Meteor. Soc.*, **123**, 657–677, https://doi.org/10.1002/qj.49712353907.

Hane, C. E., H. B. Bluestein, T. M. Crawford, M. E. Baldwin, and R. M. Rabin, 1997: Severe thunderstorm development in relation to along-dryline variablity: A case study. *Mon. Wea. Rev.*, **125**, 231–251, https://doi.org/10.1175/1520-0493(1997)125<0231:STDIRT>2.0.CO;2.

Hawkes, H. B., 1945: Mountain and valley winds. Rep. 982, Weather Division, U.S. Army Signal Corps, 44 pp.

Holton, J. R., 1967: The diurnal boundary layer wind oscillation above sloping terrain. *Tellus*, **19**, 199–205, https://doi.org/10.1111/j.2153-3490.1967.tb01473.x.

Iacono, M. J., J. S. Delamere, E. J. Mlawer, M. W. Shephard, S. A. Clough, and W. D. Collins, 2008: Radiative forcing by long-lived greenhouse gases: Calculations with the AER radiative transfer models. *J. Geophys. Res.*, **113**, D13103, https://doi.org/10.1029/2008JD009944.

Janjić, Z. I., 1994: The step-mountain eta coordinate model: Further developments of the convection, viscous sublayer, and turbulence closure schemes. *Mon. Wea. Rev.*, **122**, 927–945, https://doi.org/10.1175/1520-0493(1994)122<0927:TSMECM>2.0.CO;2.

——, 2001: Nonsingular implementation of the Mellor–Yamada level 2.5 scheme in the NCEP Meso model. NCEP Office Note 437, 61 pp., https://www.emc.ncep.noaa.gov/officenotes/newernotes/on437.pdf.

Jiang, X., N.-C. Lau, I. M. Held, and J. J. Ploshay, 2007: Mechanisms of the Great Plains low-level jet as simulated in an AGCM. *J. Atmos. Sci.*, **64**, 532–547, https://doi.org/10.1175/JAS3847.1.

Mahrt, L., 1981: The early evening boundary layer transition. *Quart. J. Roy. Meteor. Soc.*, **107**, 329–343, https://doi.org/10.1002/qj.49710745205.

Mass, C., 1982: The topographically forced diurnal circulations of western Washington State and their influence on precipitation. *Mon. Wea. Rev.*, **110**, 170–183, https://doi.org/10.1175/1520-0493(1982)110<0170:TTFDCO>2.0.CO;2.

McPherson, R. A., and Coauthors, 2007: Statewide monitoring of the mesoscale environment: A technical update on the Oklahoma Mesonet. *J. Atmos. Oceanic Technol.*, **24**, 301–321, https://doi.org/10.1175/JTECH1976.1.

Mellor, G. L., and T. Yamada, 1982: Development of a turbulence closure model for geophysical fluid problems. *Rev. Geophys.*, **20**, 851–875, https://doi.org/10.1029/RG020i004p00851.

Mesinger, F., and Coauthors, 2006: North American Regional Reanalysis. *Bull. Amer. Meteor. Soc.*, **87**, 343–360, https://doi.org/10.1175/BAMS-87-3-343.

Moisseeva, N., and D. G. Steyn, 2014: Dynamical analysis of sea-breeze hodograph rotation in Sardinia. *Atmos. Chem. Phys.*, **14**, 13 471–13 481, https://doi.org/10.5194/acp-14-13471-2014.

NCDC, 2017: Ranking of cities based on % annual possible sunshine in descending order from most to least average possible sunshine. National Centers for Environmental Information, https://www1.ncdc.noaa.gov/pub/data/ccd-data/pctposrank.txt.

Parish, T. R., and L. D. Oolman, 2010: On the role of sloping terrain in the forcing of the Great Plains low-level jet. *J. Atmos. Sci.*, **67**, 2690–2699, https://doi.org/10.1175/2010JAS3368.1.

Powers, J. G., and Coauthors, 2017: The Weather Research and Forecasting Model: Overview, system efforts, and future directions. *Bull. Amer. Meteor. Soc.*, **98**, 1717–1737, https://doi.org/10.1175/BAMS-D-15-00308.1.

Rasmussen, E. N., and D. O. Blanchard, 1998: A baseline climatology of sounding-derived supercell and tornado forecast parameters. *Wea. Forecasting*, **13**, 1148–1164, https://doi.org/10.1175/1520-0434(1998)013<1148:ABCOSD>2.0.CO;2.

Schroeder, J. L., W. S. Burgett, K. B. Haynie, I. Sonmez, G. D. Skwira, A. L. Doggett, and J. W. Lipe, 2005: The West Texas Mesonet: A technical overview. *J. Atmos. Oceanic Technol.*, **22**, 211–222, https://doi.org/10.1175/JTECH-1690.1.

Schwartz, C. S., G. S. Romine, K. R. Smith, and M. L. Weisman, 2014: Characterizing and optimizing precipitation forecasts from a convection-permitting ensemble initialized by a mesoscale ensemble Kalman filter. *Wea. Forecasting*, **29**, 1295–1318, https://doi.org/10.1175/WAF-D-13-00145.1.

——, ——, M. L. Weisman, R. A. Sobash, K. R. Fossell, K. W. Manning, and S. B. Trier, 2015: A real-time convection-allowing ensemble prediction system initialized by mesoscale ensemble Kalman filter analyses. *Wea. Forecasting*, **30**, 1158–1181, https://doi.org/10.1175/WAF-D-15-0013.1.

Segal, M., J. F. W. Purdom, J. L. Song, R. A. Pielke, and Y. Mahrer, 1986: Evaluation of cloud shading effects on the generation and modification of mesoscale circulations. *Mon. Wea. Rev.*, **114**, 1201–1212, https://doi.org/10.1175/1520-0493(1986)114<1201:EOCSEO>2.0.CO;2.

——, R. Avissar, M. C. McCumber, and R. A. Pielke, 1988: Evaluation of vegetation effects on the generation and modification of mesoscale circulations. *J. Atmos. Sci.*, **45**, 2268–2293, https://doi.org/10.1175/1520-0469(1988)045<2268:EOVEOT>2.0.CO;2.

Shapiro, A., E. Fedorovich, and S. Rahimi, 2016: A unified theory for the Great Plains nocturnal low-level jet. *J. Atmos. Sci.*, **73**, 3037–3057, https://doi.org/10.1175/JAS-D-15-0307.1.

Skamarock, W. C., and Coauthors, 2008: A description of the Advanced Regional WRF version 3. NCAR Tech. Note NCAR/TN-475+STR, 113 pp., http://www2.mmm.ucar.edu/wrf/users/docs/arw_v3.pdf.

Tang, B., M. Vaughn, R. Lazear, K. Corbosiero, L. Bosart, T. Wasula, I. Lee, and K. Lipton, 2016: Topographic and boundary influences on the 22 May 2014 Duanesburg, New York, tornadic supercell. *Wea. Forecasting*, **31**, 107–127, https://doi.org/10.1175/WAF-D-15-0101.1.

Thompson, G., P. R. Field, R. M. Rasmussen, and W. D. Hall, 2008: Explicit forecasts of winter precipitation using an improved bulk microphysics scheme. Part II: Implementation of a new snow parameterization. *Mon. Wea. Rev.*, **136**, 5095–5115, https://doi.org/10.1175/2008MWR2387.1.

Thompson, R. L., C. M. Mead, and R. Edwards, 2007: Effective storm-relative helicity and bulk shear in supercell thunderstorm environments. *Wea. Forecasting*, **22**, 102–115, https://doi.org/10.1175/WAF969.1.

Tiedtke, M., 1989: A comprehensive mass flux scheme for cumulus parameterization in large-scale models. *Mon. Wea. Rev.*, **117**, 1779–1800, https://doi.org/10.1175/1520-0493(1989)117<1779:ACMFSF>2.0.CO;2.

Torn, R. D., G. J. Hakim, and C. Snyder, 2006: Boundary conditions for limited-area ensemble Kalman filters. *Mon. Wea. Rev.*, **134**, 2490–2502, https://doi.org/10.1175/MWR3187.1.

Van de Wiel, B. J. H., A. F. Moene, G. J. Steeneveld, P. Baas, F. C. Bosveld, and A. A. Holtslag, 2010: A conceptual view on inertial oscillations and nocturnal low- low-level jets. *J. Atmos. Sci.*, **67**, 2679–2689, https://doi.org/10.1175/2010JAS3289.1.

Weber, B. L., and Coauthors, 1990: Preliminary evaluation of the first NOAA demonstration network wind profiler. *J. Atmos. Oceanic Technol.*, **7**, 909–918, https://doi.org/10.1175/1520-0426(1990)007<0909:PEOTFN>2.0.CO;2.

Weisman, M. L., and J. B. Klemp, 1982: The dependence of numerically simulated convective storms on vertical wind shear and buoyancy. *Mon. Wea. Rev.*, **110**, 504–520, https://doi.org/10.1175/1520-0493(1982)110<0504:TDONSC>2.0.CO;2.

——, and ——, 1984: The structure and classification of numerically simulated convective storms in directionally varying wind shears. *Mon. Wea. Rev.*, **112**, 2479–2498, https://doi.org/10.1175/1520-0493(1984)112<2479:TSACON>2.0.CO;2.

Zhang, C., Y. Wang, and K. Hamilton, 2011: Improved representation of boundary layer clouds over the southeast Pacific in ARW-WRF using a modified Tiedtke cumulus parameterization scheme. *Mon. Wea. Rev.*, **139**, 3489–3513, https://doi.org/10.1175/MWR-D-10-05091.1.

Zhong, S., J. D. Fast, and X. Bian, 1996: A case study of the Great Plains low-level jet using wind profiler network data and a high-resolution mesoscale model. *Mon. Wea. Rev.*, **124**, 785–806, https://doi.org/10.1175/1520-0493(1996)124<0785:ACSOTG>2.0.CO;2.